BBA Advances 5 (2024) 100113

Contents lists available at ScienceDirect

BBA Advances

journal homepage: www.sciencedirect.com/journal/bba-advances

Exploiting the full potential of cryo-EM maps

Thomas Bick [a], Paulina M. Dominiak [b], Petra Wendler [a,*]

[a] Institute of Biochemistry and Biology, Department of Biochemistry, University of Potsdam, Karl-Liebknecht Strasse 24-25, 14476 Potsdam Golm, Germany
[b] Biological and Chemical Research Centre, Faculty of Chemistry, University of Warsaw, ul. Żwirki i Wigury 101, 02-089 Warsaw, Poland

ARTICLE INFO

Keywords:
Coulomb potential
Cryo-EM
Charge
Redox proteins
Radiation damage
Fitting algorithms

ABSTRACT

The Coulomb potential maps generated by electron microscopy (EM) experiments contain not only information about the position but also about the charge state of the atom. This feature of EM maps allows the identification of specific ions and the protonation state of amino acid side chains in the sample. Here, we summarize qualitative observations of charges in EM maps, discuss the difficulties in interpreting the charge in Coulomb potential maps with respect to distinguishing it from radiation damage, and outline considerations to implement the correct charge in fitting algorithms.

Introduction

Technical developments in recent years have led to an impressive improvement in the structures derived from cryo-EM experiments, such that the average resolution of most single-particle cryo-EM structures is now between 2 Å and 4 Å. The resolution that can be achieved in X-ray crystallographic and in EM experiments is therefore comparable. Due to the intriguing scattering behaviour of electrons, EM maps contain information not only about an atom's position but also about its charge state. In an X-ray crystallographic experiment, X-ray photons are scattered by the electrons of an atom and produce electron density maps. In an electron microscope, the electron beam is scattered by the atomic Coulomb potential created by the negatively charged electron cloud and the positively charged nucleus of the atom. The resulting map from all microscopic techniques that use electron beams such as single particle cryo-EM, cryo-electron tomography or electron crystallography on 2D or 3D crystals is a Coulomb (electrostatic or electric) potential map. The contribution of each atom to the scattering, also called scattering amplitude, is described with atomic scattering factors or form factors. They depend mainly on the radiation type, the scattering angle, and the atomic number of the element. Within the most used approximation called Independent Atom Model (IAM), atomic scattering factors are derived from quantum mechanics calculations applied to isolated atoms (neutral or ionic) and are spherically symmetric. Scattering factors for biologically relevant isolated atoms have been calculated and are published in the International Tables for Crystallography [1]. The atomic scattering factors for X-rays, $f^x(\mathbf{s})$, are the Fourier transform of the electron density of the atom, $\rho(\mathbf{r})$,[1]:

$$f^x(\mathbf{s}) = \int \rho(\mathbf{r}) exp[2\pi i \mathbf{s}\cdot\mathbf{r}]\mathrm{d}\mathbf{r} \quad (1)$$

They correspond to the number of electrons in the atom. The X-ray scattering factors for light elements are relatively constant, they decrease slowly at high scattering angles (Fig. 1A). The scattering factors for electrons, $f^e(\mathbf{s})$, reflect the electrostatic potential of the atom, $\varphi(\mathbf{r})$,:

$$f^e(\mathbf{s}) = K \int \varphi(\mathbf{r}) exp[2\pi i \mathbf{s}\cdot\mathbf{r}]\mathrm{d}\mathbf{r} \quad (2)$$

with K being a multiplier. They are much more strongly influenced by the atomic charge states than X-ray scattering factors, what can be inferred from the Mott-Bethe formula:

$$f^e(\mathbf{s}) = \frac{Ke}{\varepsilon_0}\left(\frac{Z - f^x(\mathbf{s})}{s^2}\right) \quad (3)$$

Therefore, electron scattering factors for neutral atoms are qualitatively comparable to those of X-rays but differ significantly for ions (Fig. 1B) [2,3]. In particular, for small scattering angles corresponding to distances between scattering centres of 4 Å or more, the atomic charge strongly influences the appearance of the Coulomb potential map. The more positively charged an atom is, the larger the scattering amplitude at small scattering angles and the more positive the Coulomb potential map in that region (Fig. 1D, hexaaquairon ion). Negative charges, on the

* Corresponding author.
E-mail address: petra.wendler@uni-potsdam.de (P. Wendler).

https://doi.org/10.1016/j.bbadva.2024.100113
Received 5 May 2023; Received in revised form 4 January 2024; Accepted 5 January 2024
Available online 10 January 2024

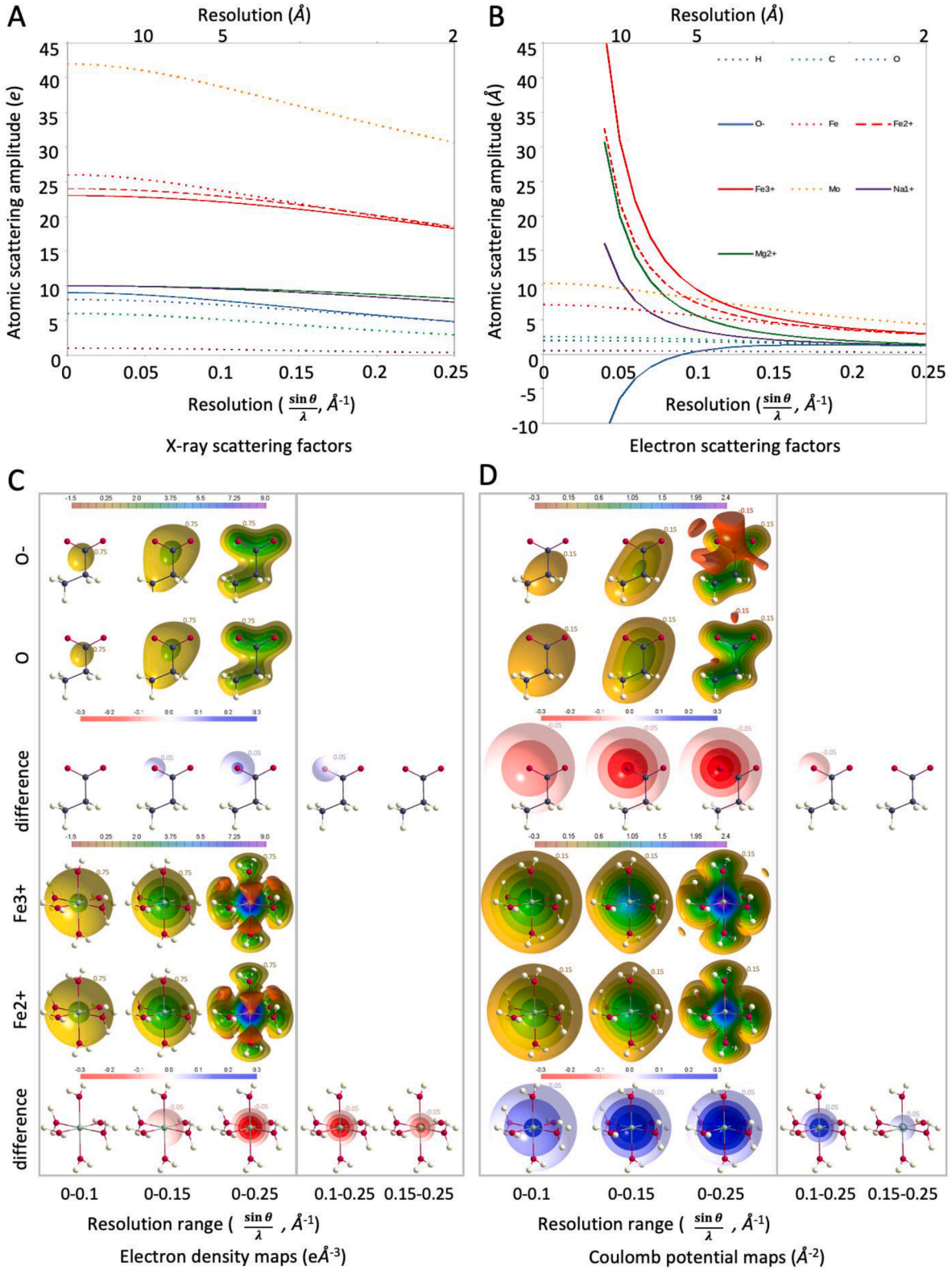

(caption on next page)

Fig. 1. Scattering factors and Fourier maps for selected neutral and ionized atoms or molecules. A, X-ray and B, electron scattering factors for selected atoms are plotted up to reciprocal resolution $\sin\theta/\lambda = 0.25$ Å^{-1} (2 Å spatial resolution) to highlight differences at low scattering angles (low values of reciprocal resolution). θ represents half the scattering angle, λ is the wavelength of the incident X-ray or electrons. Neutral atoms are depicted as dotted lines and ionized atoms as solid or dashed lines. Values were taken from the *International Tables for Crystallography Vol. C.* C, electron density and D, electrostatic potential Fourier maps computed for various ranges of reciprocal resolutions for propionate (top three rows) and hexaaquairon (bottom three rows) ions. For propionate ion, Fcalc maps computed with the O^- scattering factor assigned to the left oxygen atom and neutral scattering factors to all other atoms are shown in the top rows, Fcalc maps computed with neutral scattering factors assigned to all atoms are shown in the middle rows, and the differences between the two maps (ionized minus neutral) are shown in the bottom rows. For the hexaaquairon ion, Fcalc maps computed with the Fe^{3+} scattering factor assigned to the iron atom and neutral scattering factors to all other atoms are shown in the top rows, Fcalc maps computed with the Fe^{2+} scattering factor assigned to the iron atom and neutral scattering factors to all other atoms are shown in the middle rows, and the differences between the two maps (Fe^{3+} minus Fe^{2+}) are shown in the bottom rows. Fcalc maps for electron densities are contoured every 0.75 eÅ^{-3}, and difference maps for electron densities are contoured every 0.05 eÅ^{-3}. Fcalc maps for Coulomb potentials are contoured every 0.15 Å^{-2}, and difference maps for Coulomb potentials are contoured every 0.05 Å^{-2}. All maps are plotted on absolute scale. All maps are computed with B-factors equal to zero.

other hand, can lead to negative regions in the electron potential and invisible components in the map (Fig. 1D, propionate ion). The lower the resolution of the Coulomb potential map, the more pronounced the charge effect in the map. For example, at 5 Å resolution ($\sin\theta/\lambda$ from 0.0 to 0.1 Å^{-1}), one electron charge difference lowers the map values by more than 70 % at the position of the oxygen atom in the carboxylic group of the propionate anion or rises the values by ca. 23 % at the iron atom position in an hexaaquairon cation. At 2 Å resolution ($\sin\theta/\lambda$ from 0.0 to 0.25 Å^{-1}) corresponding percentage changes are 30 % for the oxygen and 18 % for the iron atom. This is not the case for electron density maps, for which one electron difference in scattering power is hardly visible, as it shifts the values of the map by relatively small numbers (ca. 3 %) (Fig. 1C). The contributions of scattering at small scattering angles is even more visible on high-pass filtered Fourier difference maps. When difference maps from 0.0 to 0.25 Å^{-1} resolution range (un-filtered) are compared to maps from 0.1 to 0.25 Å^{-1} and 0.15–0.25 Å^{-1} resolution ranges (filtered), the strong difference signal visible on the un-filtered map decreases with the level of filtering. This effect is more pronounced for Coulomb potential maps; the signal disappears much faster than for electron density maps.

The differences seen in the simulations (Fig. 1C and D) are expected to be smaller in experimental maps, because atoms in molecules usually bear partial charges rather than formal charges [4].

The effect of charge in EM maps

The charge dependent electron scattering behaviour in electron microscopy experiments of biological samples has been highlighted in several recent reports. They indicate how this unique property of electron beams can be exploited in different ways.

First, the exact knowledge of hydrogen positions of a biological macromolecule is indispensable for a functional understanding of catalytic reactions and protein interactions. Hydrogen atoms can be better detected in Coulomb potential maps than in electron density maps, because of the additional nuclear contribution to the scattering factors and the sensitivity to partial charges introduced by polarization. The highest resolution Coulomb potential maps obtained with single particle cryo-EM currently show clear densities for hydrogen atoms at resolutions between 1.15–1.35 Å [5–7] using apoferritin as a benchmark. Interestingly, the distances between the peak densities of hydrogen atom and its covalent bond partner in Coulomb potential maps are similar to those obtained from neutron crystallography experiments [5,6,8], reflecting the fact that neutron and electron beams are scattered by the nuclei of the bond partners [9]. In contrast, maps from X-ray experiments show only weak hydrogen densities even at 1.06 Å resolution ([7] as X-rays are scattered by the electron clouds of the atoms. Since the electron of the hydrogen atom is attracted by the parent atom, the standard refinement of electron density maps yields C—H peak distances that are about 0.1 Å shorter than those obtained from neutron diffraction experiments [10]. Only by using scattering factors beyond spherical approximation can hydrogen atoms be accurately located in X-ray datasets that scatter up to at least 0.8 Å, using for example the Hirshfeld atom refinement (HAR [10]) or the transferable aspherical atom model (TAAM) refinement [11]. Due to technical difficulties in obtaining atomic-resolution X-ray and neutron diffraction data for macromolecular crystals, experimental data showing nuclear peak distances for X-H compounds are still scarce. Further advancements in electron microscopy, sample preparation and data processing will result in more samples to be resolved to atomic resolutions up to 1.15–1.35 Å in which hydrogen-atoms are directly visible. That will allow a better understanding of hydrogen bonding networks and protein protonation states.

Secondly, protein function often depends on the charge state of amino acid side chains. For example, proton transfer across membranes is mediated by transient binding to acidic side chains in proton pumping membrane complexes. The proton transfer pathway and its regulation by cellular conditions can be deduced from the protonation state of the involved amino acids. Electron crystallographic data on Bacteriorhodopsin, a light driven proton pump from bacteria, suggested long ago that the negative charge on carboxylates of acidic side chains can be identified by weaker Coulomb potential map intensities [12,13]. Previous work on the light-harvesting chlorophyll a/b-protein complex associated with photosystem II has also observed similar effects [14]. In this work, it was proposed that positively and negatively charged amino acid side chains, reflected in stronger and weaker map density, respectively, serve as chlorophyll ligands and support the stability of the complex within the chloroplast membrane. Analysis of a high resolution apoferritin structure also indicates that delocalised charge on aspartate and glutamate side chains can be identified by the appearance of negative density when excluding high-resolution terms above 2.5 Å in the 3D reconstruction [5]. A more comprehensive review of studies utilizing the Coulomb potential to investigate the charge state of macromolecules can be found elsewhere [15]. So far, all investigations have been qualitative. Quantification of partial and complete charges on biological molecules in EM experiments would allow accurate measurement of pH and hydration effects at atomic resolution in solution and membranes. While high resolution structures are required to determine the spatial arrangement of atoms, charge information can be derived at a resolution of 3–4 Å, which is achieved in many cryo-EM reconstructions today.

Third, the detection of specific ions in single particle cryo-EM structures without prior knowledge is challenging. Traditionally, the identification of monoatomic ions is inferred from the chemical environment or by anomalous scattering in X-ray experiments [16]. Despite numerous improvements in algorithms that automatically place solvent atoms in electron density, some cases remain challenging even with current methods. Species such as OH^-, H_2O, Na^+ or Mg^{2+} have the same number of electrons and are difficult to distinguish in crystallographic electron density maps, especially at moderate resolutions (Fig. 1A). Due to their different scattering behaviour, these species can be distinguished in EM experiments (Fig. 1B) [17,18]. Here, low resolution data even need to be included in the calculations due to the strong influence of scattering amplitudes at small scattering angles [13,17]. A re-examination of recently published cryo-EM maps of the human ribosome, considering their electrostatic potential revealed that Mg^{2+}

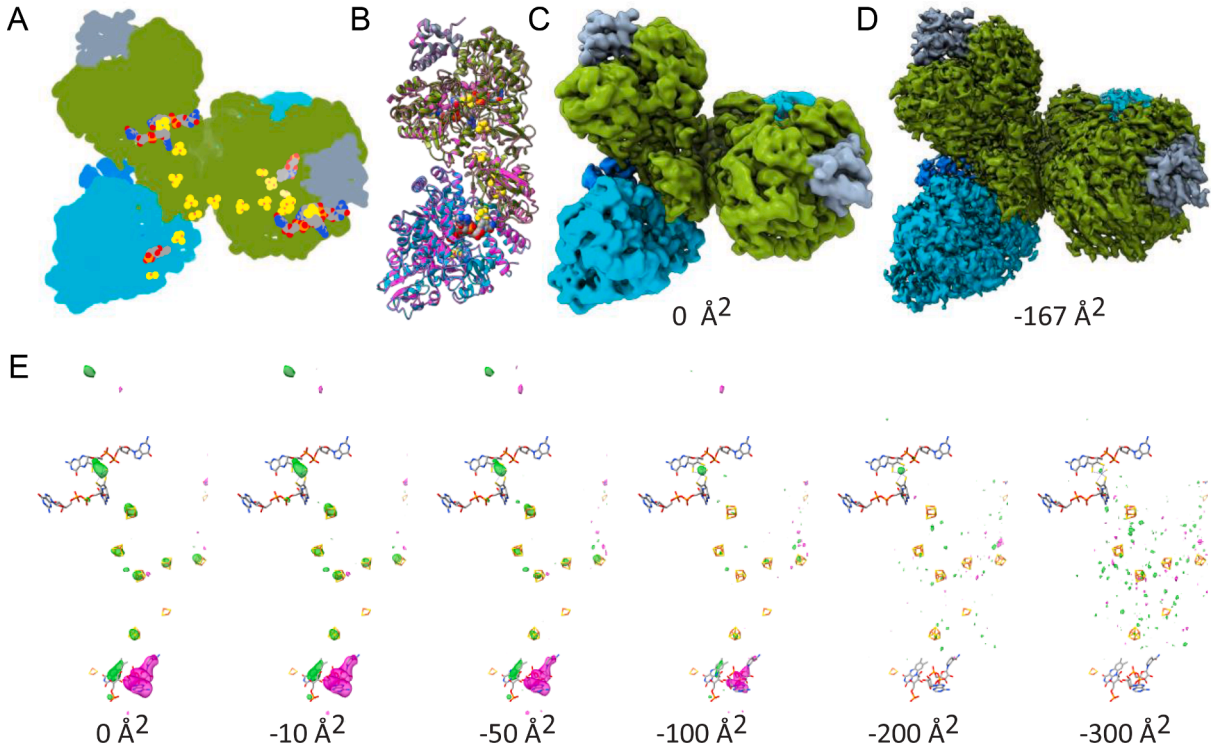

Fig. 2. Charge analysis of *Rhodobacter capsulatus* formate dehydrogenase (*Rc*FDH) [21]. A, Overall layout and location of cofactors in the *Rc*FDH dimer. FDH subunits are colour coded as follows: FdsA, green; FdsB, cyan; FdsG, blue; FdsD, grey. Bis-molybdopterin guanine dinucleotide cofactors, molybdenum, iron sulfur clusters and flavin mononucleotide are colored by element and shown in sphere representation. B, Overlay of as isolated *Rc*FDH structure and NADH reduced *Rc*FDH structure (pink). RMSD= 0.305 over 1659 residues. C, Three-dimensional reconstruction of C2 symmetric *Rc*FDH (as isolated) without b-factor sharpening (b-factor= 0 Å^2) and D, with optimal b-factor sharpening (b-factor=−167 Å^2) according to the postprocessing procedure in Relion [22]. E, Positive (green) and negative (pink) difference densities between as isolated and NADH reduced *Rc*FDH maps. B-factors used for sharpening of the maps prior to subtraction are indicated. All difference maps are shown at 18 s. Data sets for both conditions were taken with identical microscopic setup and dose. (For interpretation of the references to color in this figure legend, the reader is referred to the web version of this article.)

ions nearby nucleotide bases were previously misinterpreted as chemical modification of the bases [19].

Fourth, metals of different ionic states are used in protein complexes for structural reasons, for catalysis or for electron transfer in respiration and photosynthesis. The analysis of the charge density of polynuclear metalloproteins is particularly challenging and requires ultra-high resolution X-ray analysis [20]. Very few protein complexes form high quality crystals for such analysis, hence many structures need to be interpreted at lower resolution using strong restraints during refinement calculations which makes the interpretation of redox states difficult if not impossible. In Coulomb potential maps ionic states of metals can already be distinguished at moderate resolutions between 2.5 Å and 4 Å due to the differences in their scattering behaviour. For example, the scattering amplitude of Fe^{2+} at very small scattering angles is only 66 % of that of Fe^{3+} [1] resulting in about 20 % difference in the density peak height of Coulomb potential maps. Instead of interpreting charge by comparing an experimental Coulomb potential map with a theoretical map including the corresponding charges, it is also possible to derive charge states qualitatively by comparing two maps obtained under identical experimental conditions. We have recently shown that cryo-EM analysis of two different redox states of the molybdoenzyme formate dehydrogenase from *Rhodobacter capsulatus* reveals difference densities on various co-factors of the protein, corresponding to a reduction of metal ions by the introduced electrons in one of the states [21] (Fig. 2). When the maps are B-factor sharpened to attenuate the low-resolution frequencies and minimise the effect of the different scattering amplitudes, the signal in the difference maps disappears. This work indicates that the difference in scattering behaviour between Fe^{2+} and Fe^{3+}allows visualisation of single electrons on iron sulphur clusters even at an average resolution of 3.6 Å, when both maps are obtained under identical experimental conditions. The qualitative assessment of our work suggests that electrons are preferentially located on certain iron atoms in some iron sulphur clusters. A quantitative assessment of charge on metal-cofactors would provide information on the residence time of electrons on co-factors and could be used, for example, to determine the redox potential of iron sulphur clusters under certain environmental conditions. As argued below, quantification of these effects using Coulomb potential maps is not trivial. Since single particle analysis allows the selection of only intact protein complexes in the sample, these analyses of charge differences could be more accurate than those that average the entire population of protein complexes in a sample such as electron paramagnetic resonance spectroscopy (EPR).

Radiation damage shows similar effects to charge in EM maps

Unfortunately, charge dependent scattering differences in Coulomb potential maps are barely distinguishable from specimen damage introduced by radiation. Both, X-rays and electrons cause radiation damage by inelastic scattering. In this process, an electron is ejected from the atom, which can cause further damage through additional ionization events in neighbouring atoms. The ejected electrons are mobile even at a temperature of 77 K and are efficiently captured at electrophilic sites such as Cu(II), Fe(III) or disulphide bonds [23]. Primary and secondary damage leads to chemical and conformational changes in the protein under investigation and ultimately limits the achievable resolution in the experiment. The extend of radiation damage depends on the structure of the sample, the buffer composition, the temperature at which the measurement is performed, the radiation source and its intensity. For X-rays, the extent of damage per useful elastic scattering event is several hundred times greater than for

electrons at all wavelength and energies [24]. Numerous studies have established that protein crystals at 100 K exhibit a specific order of susceptibility to damage: reduction of metal centres, cleavage of disulphide bonds, decarboxylation of acidic residues, disordering of tyrosine —OH groups, and cleavage of methionine S—C bonds (reviewed in [25]). The absorbed energy, or dose accumulated by the crystal, in this type of experiment is of the order of several MGy, with damage to photosensitive active sites and disulphide bridges being detected at doses as low as 0.06 MGy and less than 1 MGy, respectively (reviewed in [25]). In a single particle EM experiment, the dose absorbed by a specimen can only be estimated as it depends on parameters such as protein concentration, buffer type and sample thickness. Therefore, radiation damage is often described by loss of resolution or loss of side chain features at integrated flux densities. Nowadays, cryo-EM experiments with direct electron detectors record dose fractionated movies with total integrated flux densities of up to 40 to 60 e-/Å^2 corresponding to an estimated absorbed energy of 40–60 MGy for 100 keV electrons [26]. Single-frame reconstructions of the human $GABA_A$ receptor at atomic resolution allow visualisation of the dose-dependent evolution of radiation damage [6]. They show disulfide bond breakage and loss of carboxyl groups in acidic side chains after an accumulated dose of approximately 5 e-/Å^2. Interestingly, electron diffraction experiments on 3D microcrystals of proteinase K indicate that radiation damage detectable by the loss of disulphide bonds and density of acidic side chains begins at accumulated doses as low as 1 e-/Å^2 [27]. This discrepancy in minimum tolerable dose between the single particle and crystallographic EM methods could be explained by differences in data acquisition and image processing procedures that make single particle cryo-EM less sensitive to high-resolution site-specific damage [28]. It is also worth noting that the initial single-frame reconstructions of the $GABA_A$ receptor were of relatively poor quality due to sample movement, making it difficult to assess the onset of damage. Recent studies of dose-dependent charge effects on acidic side chain residues revealed no apparent radiation damage when difference maps for 2, 3, 20 and 40 e-/Å^2 doses at resolutions up to 3 Å were analysed using dose-weighted movie frame summation [5]. Novel approaches to achieve movement-free imaging allow extrapolation to a map of the specimen at zero electron irradiation to reconstruct the undamaged structure [29]. Separating map features arising from radiation and those arising from scattering due to Coulomb potential would be particularly useful when quantifying charge-dependent map features.

Implementation of charge in fitting algorithms

In principle, charge dependent effects in scattering amplitudes can be quantified by minimizing the differences between an experimental Coulomb potential map and a theoretical map taking charged atoms into account. This routine could be integrated into fitting procedures for building atomic models from cryo-EM structures, which have been continuously improved in recent years [30]. However, the calculation of a theoretical map is not trivial, as aspects such as local resolution of the map or the deviation of scattering factors from the theoretical values due to bonding interactions of the atoms need to be considered [31,32].

Negative difference densities between the experimental map and a theoretical map assuming neutral atoms can be attributed to either negatively charged atoms, radiation damage or local flexibility. A quantification of charge is only possible if the contribution of radiation damage and flexibility to weak map densities is taken into account. Recently, the contribution of radiation damage could be extrapolated from maps derived from movement-free data [29] while local flexibility can be estimated using, among other tools, the Q-score, a measure of resolvability at side chain level [33]. Positive difference densities, on the other hand, can originate exclusively from positively charged atoms, provided that the model includes all atoms of the protein complex under investigation and atomic displacement parameters (B-factors) are properly estimated. However, quantifying positive charge which is frequently found on bound metal ions is challenging because the occupancy of metal binding sites can vary considerably in the averaged data of a 3D reconstruction.

Nevertheless, some attempts have been made to quantify charge. Yonekura and co-workers have used electron scattering factors calculated for isolated atoms and augmented with partial charge [18]. By iteratively performing refinements of the atomic model with partial charges varied in small steps, they were able to identify charge distributions that yielded the best model-fitting statistics. Direct refinement of the charge population along with refinement of the atomic model using experimental EM data of biomacromolecules has not yet been implemented in any publicly available software.

In fact, modelling partial charges on atoms already represents a simplification of the situation. The distribution of electronic charge on atoms in molecules is not spherical due to anisotropic bonding interactions. Hence, the widely used IAM disregards the fact that the scattering amplitudes for atoms in molecules may depend strongly on the direction of the scattering vector. The change in orientation of one single p orbital with regard to the scattering vector can change the total electron scattering factor by 5–10 % in comparison to a spherical scattering factor [34]. A more accurate calculation of structure factors would therefore need to include an *ab initio* assessment of the molecular electrostatic potential [35], which is currently computationally infeasible for large protein complexes. The superposition of potentials calculated for small fragments has been tested for different conformations of N-acetylalanine methylamide and a reduction of the calculated R-factors by 5–15 % in the resolution range of 2.5–25 Å [35] was obtained.

In X-ray crystallography, the concept of computing the structure factors from *ab initio* derived molecular electron densities was implemented in the HAR [10] and references cited therein). Libraries of atomic fragment electron densities were also created [36,37], including biologically relevant atom types. The atomic electron densities are expressed using multipolar expansion up to hexadecapolar level. The libraries are being applied in the TAAM refinements [11]. HAR and TAAM are now becoming popular in small-molecule X-ray crystallography, for macromolecules some proof-of-concept results were also published [38,39]. In case of sub-atomic resolution X-ray diffraction for macromolecules, it was shown that it is even possible to refine electron density parameters of multipole model directly on experimental data [20,40].

Recently, TAAM refinement was adapted for electron crystallography [4,8] and evaluated for small molecule crystals. Clearly, TAAM can fit Coulomb potential maps much better than the standard spherical IAM. The effects of application of TAAM refinement to biomacromolecules are not fully explored yet [31], not to mention direct refinement of multipole model on Coulomb potential maps (neither in real nor in reciprocal space).

The shortcomings of a theoretical modelling of macromolecules may be overcome by creation of difference maps between two Coulomb potential maps obtained under different physiological conditions but identical microscopic setup, as shown for the FDH complex [21]. However, false positive or false negative assignments can occur when the two maps are from different experimental setups. Parameters such as discrepancies in the scaling of maps [41], the microscopic setup and the integrated electron flux densities need to be considered. Furthermore, such analysis should include a quantification of atom resolvability on side chain level using Q-scores which provide a means to compare structural features of maps derived from different experimental set-ups [33,42]. In summary, Coulomb potential maps allow the qualitative identification of the charge of amino acid side chains or bound metal ions and co-factors, but the quantification of this charge could not yet be demonstrated with the current state of the art of EM methods.

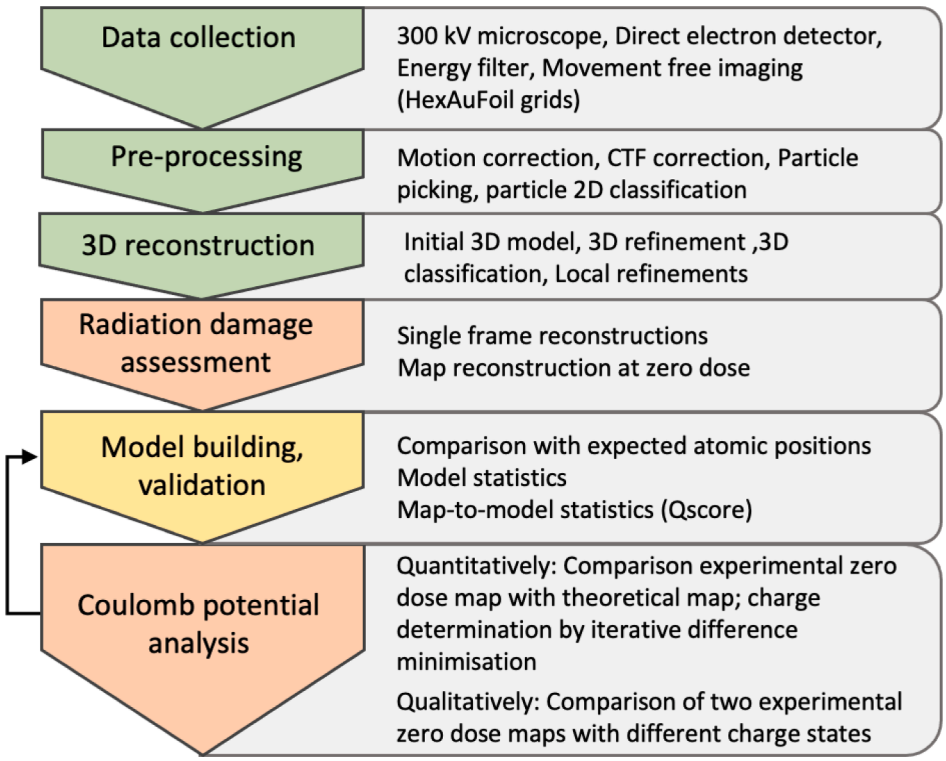

Fig. 3. Proposed workflow for determination of charge characteristics in Coulomb potential maps from SPA EM experiments. Fully validated processes are depicted in green, those which are partly or not validated are depicted in yellow and red, respectively. (For interpretation of the references to color in this figure legend, the reader is referred to the web version of this article.)

Experimental Coulomb potential analysis workflow

To date, there is no validated workflow or software tool that allows for qualitative or quantitative interpretation of charge in EM maps, but several measures can facilitate the quantification of radiation damage and charges in future experiments. We have outlined a potential path to fully integrating charge into the interpretation of EM maps in Fig. 3. For example, it would be extremely helpful to systematically record radiation damage under different experimental conditions for maps with as high a resolution as possible, so that their dependence on flux densities, grid type, sample density, data set size, microscope settings and the like can be determined. Since thin carbon or graphene oxide layers could efficiently dissipate the ejected electrons, it is possible that grids with such support minimise radiation damage to the protein, while an ice layer or even a crystalline protein structure is more susceptible to radiation damage in EM. In all experiments where charge is to be quantified, an energy filter should be used to filter out inelastically scattered electrons and reduce background noise. Ideally, a movement free data-collection should be attempted to calculate a zero-dose map without beam damage at atomic resolution. Therefore, sample freezing should be done on gold-gold grids with the smallest available hole size. To routinely achieve zero-dose maps, a software implementation to easily calculate 3D density maps from individual movie frames of the same motion corrected movie stack would be useful. The above-mentioned studies could be done with co-factor containing model protein complexes under defined biochemical conditions, which have been characterised by EPR. Any quantification must consider that metal centres, disulphide bridges, and acidic amino acid side chains are differently susceptible to radiation damage. Once radiation damage and movement during imaging are corrected for, such model protein study allows for normalisation and quantification of strong and weak densities in the EM map compared to a calculated Coulomb potential map with known charge.

Conclusion and outlook

So far, there is no proof-of-principle study that could unambiguously show a quantification of charge in EM maps, because multiple effects interfere with each other during map generation. Radiation damage, particle movement during imaging and charge effects must be dissected experimentally in order to unambiguously assign density to charge in the molecule. With the evolution of cryo-EM towards higher resolution structures for *de novo* structure elucidation, with the establishment of standards for data recording and map interpretation, and with improvements in atomic model building, it should be possible in the near future to routinely include charge in atomic models of Coulomb potential maps. Developments in the refinement procedures and in the interpretation of cryo-EM maps, utilising deep learning could expedite modelling of charge in Coulomb potential maps. This will not only improve our understanding of the function of reversibly charged residues in protein interactions and catalytic mechanisms, but also allow us to realise the full potential of cryo-EM experiments.

CRediT authorship contribution statement

Thomas Bick: Conceptualization, Visualization, Writing – review & editing. **Paulina M. Dominiak:** Conceptualization, Data curation, Formal analysis, Methodology, Visualization, Writing – review & editing. **Petra Wendler:** Conceptualization, Data curation, Formal analysis, Funding acquisition, Methodology, Project administration, Supervision, Visualization, Writing – original draft.

Declaration of competing interest

The authors declare that they have no known competing financial interests or personal relationships that could have appeared to influence the work reported in this paper.

Data availability

No data was used for the research described in the article.

Acknowledgements

This work was supported by the Deutsche Forschungsgemeinschaft (DFG, German Research Foundation) under Germany´s Excellence Strategy – EXC 2008 – 390540038 – UniSysCat. (to P.W.). We would like to thank M.Dominiak for his help in the preparation of Fig. 1.

References

[1] C. Colliex, et al., Electron diffraction. International Tables for Crystallography, International Union of Crystallography, Chester, England, 2006, pp. 259–429, https://doi.org/10.1107/9780955360206000593.
[2] L.-M. Peng, Electron scattering factors of ions and their parameterization, Acta Crystallogr. Sect. A 54 (4) (1998) 481–485, https://doi.org/10.1107/S0108767398001901.
[3] K. Yonekura, et al., Ionic scattering factors of atoms that compose biological molecules, IUCrJ 5 (Pt 3) (2018) 348–353, https://doi.org/10.1107/S2052252518005237.
[4] K.K. Jha, B. Gruza, M.L. Chodkiewicz, C. Jelsch, P.M. Dominiak, Refinements on electron diffraction data of β-glycine in *MoPro* : a quest for an improved structure model, J. Appl. Crystallogr. 54 (4) (2021) 1234–1243, https://doi.org/10.1107/S160057672100580X.
[5] S. Maki-Yonekura, K. Kawakami, T. Hamaguchi, K. Takaba, K. Yonekura, Measurment of charges and chemical bonding in a cryo-EM structure, Commun. Chem. 6 (1) (2023) 98, https://doi.org/10.1038/s42004-023-00900-x.
[6] T. Nakane, et al., Single-particle cryo-EM at atomic resolution, Nature 587 (7832) (2020) 152–156, https://doi.org/10.1038/s41586-020-2829-0.
[7] K.M. Yip, N. Fischer, E. Paknia, A. Chari, H. Stark, Atomic-resolution protein structure determination by cryo-EM, Nature 587 (7832) (2020) 157–161, https://doi.org/10.1038/s41586-020-2833-4.
[8] B. Gruza, M.L. Chodkiewicz, J. Krzeszczakowska, P.M. Dominiak, Refinement of organic crystal structures with multipolar electron scattering factors, Acta Crystallogr. Sect. A 76 (1) (2020) 92–109, https://doi.org/10.1107/S2053273319015304.
[9] C.J. Williams, et al., MolProbity: more and better reference data for improved all-atom structure validation, Protein Sci. 27 (1) (2018) 293–315, https://doi.org/10.1002/pro.3330.
[10] M. Woinska, S. Grabowsky, P.M. Dominiak, K. Wozniak, D. Jayatilaka, Hydrogen atoms can be located accurately and precisely by x-ray crystallography, Sci. Adv. 2 (5) (2016) e1600192, https://doi.org/10.1126/sciadv.1600192.
[11] K.K. Jha, B. Gruza, P. Kumar, M.L. Chodkiewicz, P.M. Dominiak, TAAM: a reliable and user friendly tool for hydrogen-atom location using routine X-ray diffraction data, Acta Crystallogr. Sect. B 76 (3) (2020) 296–306, https://doi.org/10.1107/S2052520620002917.
[12] Y. Kimura, et al., Surface of bacteriorhodopsin revealed by high-resolution electron crystallography, Nature 389 (6647) (1997) 206–211, https://doi.org/10.1038/38323.
[13] K. Mitsuoka, et al., The structure of bacteriorhodopsin at 3.0 A resolution based on electron crystallography: implication of the charge distribution, J. Mol. Biol. 286 (3) (1999) 861–882, https://doi.org/10.1006/jmbi.1998.2529.
[14] W. Kühlbrandt, D.N. Wang, Y. Fujiyoshi, Atomic model of plant light-harvesting complex by electron crystallography, Nature 367 (6464) (1994) 614–621, https://doi.org/10.1038/367614a0.
[15] M.A. Marques, M.D. Purdy, M. Yeager, CryoEM maps are full of potential, Curr. Opin. Struct. Biol. 58 (2019) 214–223, https://doi.org/10.1016/j.sbi.2019.04.006.
[16] N. Echols, et al., Automated identification of elemental ions in macromolecular crystal structures, Acta. Crystallogr. D. 70 (Pt 4) (2014) 1104–1114, https://doi.org/10.1107/S1399004714001308.
[17] J. Wang, Z. Liu, J. Frank, P.B. Moore, Identification of ions in experimental electrostatic potential maps, IUCrJ 5 (Pt 4) (2018) 375–381, https://doi.org/10.1107/S2052252518006292.
[18] K. Yonekura, S. Maki-Yonekura, Refinement of cryo-EM structures using scattering factors of charged atoms, J. Appl. Crystallogr. 49 (5) (2016) 1517–1523, https://doi.org/10.1107/S1600576716011274.
[19] J. Wang, S.K. Natchiar, P.B. Moore, B.P. Klaholz, Identification of Mg(2+) ions next to nucleotides in cryo-EM maps using electrostatic potential maps, Acta Crystallogr. D 77 (Pt 4) (2021) 534–539, https://doi.org/10.1107/S2059798321001893.
[20] Y. Hirano, K. Takeda, K. Miki, Charge-density analysis of an iron-sulfur protein at an ultra-high resolution of 0.48 A, Nature 534 (7606) (2016) 281–284, https://doi.org/10.1038/nature18001.
[21] C. Radon, et al., Cryo-EM structures reveal intricate Fe-S cluster arrangement and charging in Rhodobacter capsulatus formate dehydrogenase, Nat. Commun. 11 (1) (2020), https://doi.org/10.1038/s41467-020-15614-0.
[22] J. Zivanov, et al., New tools for automated high-resolution cryo-EM structure determination in RELION-3, eLife 7 (2018), https://doi.org/10.7554/eLife.42166.
[23] G.D. Jones, J.S. Lea, M.C. Symons, F.A. Taiwo, Structure and mobility of electron gain and loss centres in proteins, Nature 330 (6150) (1987) 772–773, https://doi.org/10.1038/330772a0.
[24] R. Henderson, The potential and limitations of neutrons, electrons and X-rays for atomic resolution microscopy of unstained biological molecules, Q. Rev. Biophys. 28 (2) (1995) 171–193, https://doi.org/10.1017/s003358350000305x.
[25] C.S. Bury, I. Carmichael, J.E. McGeehan, E.F. Garman, Radiation damage within nucleoprotein complexes studied by macromolecular X-ray crystallography, Radiat. Phys. Chem. 128 (2016) 118–125, https://doi.org/10.1016/j.radphyschem.2016.05.023.
[26] R. Henderson, B.C. Clarke, Cryo-protection of protein crystals against radiation damage in electron and X-ray diffraction, Proc. R. Soc. Lond. B 241 (1300) (1990) 6–8, https://doi.org/10.1098/rspb.1990.0057.
[27] J. Hattne, et al., Analysis of global and site-specific radiation damage in cryo-EM, Structure 26 (5) (2018), https://doi.org/10.1016/j.str.2018.03.021, 759–766 e4.
[28] D. Shi, R. Huang, Analysis and comparison of electron radiation damage assessments in Cryo-EM by single particle analysis and micro-crystal electron diffraction, Front Mol. Biosci. 9 (2022) 988928, https://doi.org/10.3389/fmolb.2022.988928.
[29] K. Naydenova, P. Jia, C.J. Russo, Cryo-EM with sub-1 A specimen movement, Science 370 (6513) (2020) 223–226, https://doi.org/10.1126/science.abb7927.
[30] M. Beckers, D. Mann, C. Sachse, Structural interpretation of cryo-EM image reconstructions, Prog. Biophys. Mol. Biol. 160 (2021) 26–36, https://doi.org/10.1016/j.pbiomolbio.2020.07.004.
[31] M. Kulik, M.L. Chodkiewicz, P.M. Dominiak, Theoretical 3D electron diffraction electrostatic potential maps of proteins modeled with a multipolar pseudoatom data bank, Acta Crystallogr. Sect. D 78 (8) (2022) 1010–1020, https://doi.org/10.1107/S2059798322005836.
[32] J. Wang, On contribution of known atomic partial charges of protein backbone in electrostatic potential density maps, Protein Sci. 26 (6) (2017) 1098–1104, https://doi.org/10.1002/pro.3169.
[33] G. Pintilie, K. Zhang, Z. Su, S. Li, M.F. Schmid, W. Chiu, Measurement of atom resolvability in cryo-EM maps with Q-scores, Nat. Methods 17 (3) (2020) 328–334, https://doi.org/10.1038/s41592-020-0731-1.
[34] J.-C. Zheng, L. Wu, Y. Zhu, Aspherical electron scattering factors and their parameterizations for elements from H to Xe, J. Appl. Crystallogr. 42 (6) (2009) 1043–1053, https://doi.org/10.1107/S0021889809033147.
[35] S. Zhong, V.M. Dadarlat, R.M. Glaeser, T. Head-Gordon, K.H. Downing, Modeling chemical bonding effects for protein electron crystallography: the transferable fragmental electrostatic potential (TFESP) method, Acta Crystallogr. Sect. A 58 (2) (2002) 162–170, https://doi.org/10.1107/S0108767301020256.
[36] K.K. Jha, B. Gruza, A. Sypko, P. Kumar, M.L. Chodkiewicz, P.M. Dominiak, Multipolar Atom Types from Theory and Statistical Clustering (MATTS) data bank: restructurization and extension of UBDB, J. Chem. Inf. Model. 62 (16) (2022) 3752–3765, https://doi.org/10.1021/acs.jcim.2c00144.
[37] M. Kulik, P.M. Dominiak, Electron density is not spherical: the many applications of the transferable aspherical atom model, Comput. Struct. Biotechnol. J. 20 (2022) 6237–6243, https://doi.org/10.1016/j.csbj.2022.10.018.
[38] D. Liebschner, et al., Elucidation of the phosphate binding mode of DING proteins revealed by subangstrom X-ray crystallography, J. Am. Chem. Soc. 131 (22) (2009) 7879–7886, https://doi.org/10.1021/ja901900y.
[39] L.A. Malaspina, et al., Fast and accurate quantum crystallography: from small to large, from light to heavy, J. Phys. Chem. Lett. 10 (22) (2019) 6973–6982, https://doi.org/10.1021/acs.jpclett.9b02646.
[40] N. Muzet, B. Guillot, C. Jelsch, E. Howard, C. Lecomte, Electrostatic complementarity in an aldose reductase complex from ultra-high-resolution crystallography and first-principles calculations, Proc. Natl. Acad. Sci. 100 (15) (2003) 8742–8747, https://doi.org/10.1073/pnas.1432955100.
[41] J. Wang, et al., How to correct relative voxel scale factors for calculations of vector-difference Fourier maps in cryo-EM, J. Struct. Biol. 214 (4) (2022) 107902, https://doi.org/10.1016/j.jsb.2022.107902.
[42] C.F. Hryc, et al., Accurate model annotation of a near-atomic resolution cryo-EM map, Proc. Natl. Acad. Sci. USA. 114 (12) (2017) 3103–3108, https://doi.org/10.1073/pnas.1621152114.